JOURNAL OF MATERIALS SCIENCE 35 (2000) 4635–4647

Crystal plasticity analysis of stress–assisted martensitic transformation in Ti–10V–2Fe–3Al (wt.%)

M. GRUJICIC, Y. ZHANG
Program in Materials Science and Engineering, Department of Mechanical Engineering, Clemson University, Clemson, SC 29634, USA
E-mail: mica@ces.clemson.edu

A new model based on crystal–plasticity, crystallography, thermodynamics, kinetics and statistics is developed for stress–assisted martensitic transformation. The model includes the essential features of the stress–assisted martensitic transformation, such as: nuclei of progressively lower potency are activated in the course of transformation, the martensite phase appears in the form of thin plates, the parent phase exerts a higher resistance toward the growth of a plate in the thickness than in the radial direction, the average plate size decreases while the average plate aspect ratio increases with the extent of transformation, etc. The model is implemented in the commercial finite element code ABAQUS/Standard to analyze the evolution of martensite, materials texture and the resulting equivalent stress–equivalent strain curve during the stress–assisted martensitic transformation under different stress and strain states in a polycrystalline Ti–10V–2Fe–3Al (wt.%) alloy. The equivalent stress–equivalent strain curves and the volume fraction of martensite–equivalent strain curves are found to be mainly controlled by the applied stress state. Conversely, the texture observed in the transformed Ti–10V–2Fe–3Al is found to be primarily controlled by the imposed macroscopic strain state. The validity of the proposed materials constitutive model has been established by demonstrating a reasonable agreement between the model predictions and the available experimental data.

1. Introduction

Martensitic transformation is generally characterized as a diffusionless, displacive change in materials crystal structure in which both the morphology of the product phase (martensite) and the kinetics of the transformation process are dominated by the strain accompanying the transformation. In general, martensitic transformation begins to take place spontaneously during (fast) cooling from elevated temperatures when the temperature falls below a material–specific temperature, M_s (the martensite start temperature). The transformation product generally consists of coarse plates. Martensitic transformation, however, can take place at temperatures above M_s provided an external stress is applied. At temperatures between M_s and a stress–state dependent temperature generally referred to as M_s^σ, martensite appears also in the form of coarse plates. It is believed that in this temperature range the applied stress merely assists the formation of martensite plates at the same nucleation sites which give rise to the formation of martensite plates on cooling below M_s. Consequently, the martensitic transformation taking place in the M_s–M_s^σ temperature range is named the "stress–assisted" martensitic transformation [1]. Since the chemical driving force (the difference in the Gibbs free energies of the parent phase and martensite) becomes smaller and eventually becomes negative as temperature increases, the stress required for the onset of martensitic transformation in the stress–assisted regime increases with temperature. At temperatures above M_s^σ, the stress needed to initiate the transformation becomes higher than the parent–phase yield stress. Consequently, the applied stress causes plastic deformation (typically by slip) rather than the martensitic transformation to take place. Nonuniformity in plastic deformation gives rise to the formation of various planar– and volume–type lattice defects such as stacking faults, shear bands, twins, etc. The places where these defects intersect act as additional potential sites for the nucleation of martensite plates. Combined effects of the additional nucleation sites and the applied stress cause the martensitic transformation to take place after a certain amount of plastic deformation. This type of martensitic transformation is generally referred to as the "strain–induced" martensitic transformation [1] and is characterized by a very fine–plate martensite microstructure. The strain–induced martensitic transformation is generally observed up to a stress state–dependent temperature M_d, above which failure occurs before any transformation takes place.

During the last two decades, it has been unequivocally established that the stress–assisted martensitic transformation can significantly enhance the tensile ductility and the fracture toughness of high–strength, brittle materials. The martensitic transformation has been most extensively investigated and the major improvements in ductility and toughness obtained in ZrO_2 and various ceramics containing ZrO_2 second–phase particles (e.g. [2]), in ultra–high strength secondary–hardening steels (e.g. [3]) and in γ–TiAl intermetallic containing metastable dispersions of Ti–V–based precipitates [4].

Over the last ten years, several constitutive models for materials undergoing a stress–assisted transformation have been proposed. Several of them (e.g. [5, 6]) are quite simple and purely phenomenological in nature. Others (e.g. [7, 8]) are more sophisticated and take into account the basic thermodynamics, kinetics, statistics and heterogeneous nature of the martensitic transformation. However, in all these models, the material is considered as a latticeless continuum, and hence no account can be given to the basic crystallography of martensitic transformation.

In the present work, we proposed a new crystal–plasticity based model for the stress–assisted martensitic transformation. The model utilizes the approach for incorporation of deformation twinning in crystal plasticity recently proposed by Kalidindi [9]. The model is subsequently used to analyze the evolution of martensite and materials texture and their effect on the stress–strain curves associated with a b.c.c.→f.c.o. stress–assisted martensitic transformation in Ti–10V–2Fe–3Al (wt.%) under uniaxial and plane–strain compression and bi–axial tension.

The organization of the paper is as following. The development of the materials constitutive model including the derivation of the evolution for the transformation resistance is presented in Section 2. The application of the model to the stress–assisted b.c.c.→f.c.o. martensitic transformation in the Ti–10V–2Fe–3Al (wt.%) alloy under uniaxial and plane–strain compression as well as under bi–axial tension is discussed in the Section 3. Main conclusions resulted from the present work are presented in Section 4.

2. Material constitutive model

Notation used in the present work is based on the following conventions: Scalars are written in italic type (e.g. γ, σ, f), vectors using boldface lowercase Romans (e.g. **n**, **m**), second order tensors as boldface uppercase Romans (e.g. **F**, **T**, **E**), while fourth order tensor using capital boldface italics (e.g. ***L***). The tensor (dyadic) product is indicated by "⊗", while the scalar product of the tensors of appropriate order by a raised dot.

2.1. Derivation

The main feature of the present model is that the inelastic deformation of the material takes place by a transformation of the parent–material crystal structure into the crystal structure of martensite phase and that the martensite phase can appear in several crystallographically–equivalent variants. In addition to the inelastic deformation, the crystal lattices of the two structures along with the embedded material undergo elastic deformation and rotation. Consequently, the total deformation gradient **F** is multiplicative decomposed as:

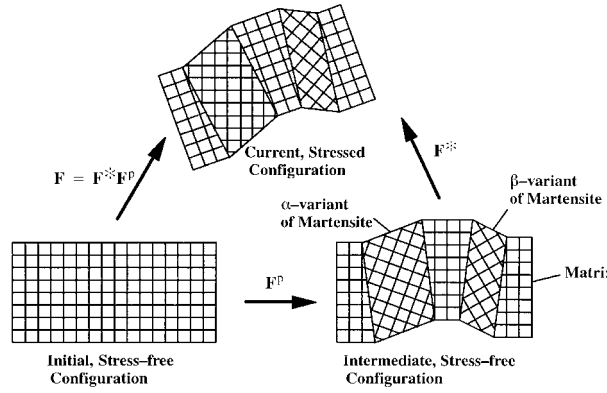

Figure 1 Decomposition of the deformation gradient for a material undergoing a stress–assisted martensitic transformation.

$$\mathbf{F} = \mathbf{F}^{*}\mathbf{F}^{\mathrm{p}} \tag{1}$$

where $\mathbf{F}^{*}$ and $\mathbf{F}^{\mathrm{p}}$ are respectively the elastic and the plastic components of **F**. A schematic of the multiplicative decomposition of the deformation gradient as defined in Equation 1 is shown in Fig. 1. For clarity only two variants of martensite are shown in Fig. 1.

While Fig. 1 shows that only some regions of the crystal undergo inelastic deformation, the crystal is homogenized in the present model so that each portion of the crystal is taken to undergo the same deformation gradient, an effective deformation gradient defined as the weighted contribution of the deformation gradient of different parts of the crystal. Since the deformation gradient is made uniform throughout the crystal, the stresses in its different parts can be defined as:

$$\mathbf{T}^{*\mathrm{pt}} = \boldsymbol{L}^{\mathrm{pt}}[\mathbf{E}^{*}] \tag{2}$$

$$\mathbf{T}^{*\alpha-\mathrm{mt}} = \boldsymbol{L}^{\alpha-\mathrm{mt}}[\mathbf{E}^{*}] \tag{3}$$

where ***L*** is the fourth–order elasticity tensor, $\mathbf{T}^{*}$ and $\mathbf{E}^{*}$ represent respectively the second Piolla–Kirchhoff stress and the Green strain, and the superscripts "pt" and "$\alpha-$mt" refer respectively to the parent phase and the α–variant of martensite. $\mathbf{T}^{*}$ and $\mathbf{E}^{*}$ are defined respectively by the following two relations:

$$\mathbf{T}^{*} = \mathbf{F}^{*-1}\{(\det \mathbf{F}^{*})\mathbf{T}\}\mathbf{F}^{*-\mathrm{T}} \tag{4}$$

$$\mathbf{E}^{*} = \left(\frac{1}{2}\right)\{\mathbf{F}^{*\mathrm{T}}\mathbf{F}^{*} - \mathbf{I}\} \tag{5}$$

where **T** is the Cauchy stress, **I** the second order identity tensor and "det" and superscript "T" denote the determinant and the transpose, respectively. The Cauchy stress in the crystal is defined as a volume average of

the stresses in its various parts as:

$$\mathbf{T} = \left(1 - \sum_{\alpha} f^{\alpha}\right)\mathbf{T}^{\mathrm{pt}} + \sum_{\alpha} f^{\alpha}\mathbf{T}^{\alpha-\mathrm{mt}} \tag{6}$$

where f^{α} denotes the volume fraction of the α–variant of martensite.

Following Asaro and Needleman [10], the evolution of the plastic deformation gradient is defined as:

$$\dot{\mathbf{F}}^{\mathrm{p}} = \mathbf{L}^{\mathrm{p}}\mathbf{F}^{\mathrm{p}} \tag{7}$$

where the raised dot in $\dot{\mathbf{F}}^{\mathrm{p}}$ denotes a time derivative of $\mathbf{F}^{\mathrm{p}}$ and the plastic velocity gradient $\mathbf{L}^{\mathrm{p}}$ can be expressed as:

$$\mathbf{L}^{\mathrm{p}} = \left(1 - \sum_{\alpha} f^{\alpha}\right)\sum_{\alpha} \dot{f}^{\alpha}\gamma^{\alpha-\mathrm{mt}}\left(\mathbf{S}^{\alpha} + \frac{\varepsilon_n^{\mathrm{mt}}}{\gamma^{\alpha-\mathrm{mt}}}\mathbf{I}\right) \tag{8}$$

where $\gamma^{\alpha-\mathrm{mt}}$ denotes the transformation shear strain associated with the α–variant of martensite and $\varepsilon_n^{\mathrm{mt}}$ the transformation volume change. It should be noted that according to Equation 8, stress assisted martensitic transformation is the sole mode of inelastic deformation. Consequently, the model developed here is strictly applicable only at lower stress levels at which martensitic transformation proceeds by activation of the highly potent nuclei. Contrary, near completion of martensitic transformation high stress levels are required to activate less potent nuclei. Under such conditions, other modes of inelastic deformation may become operational and the present model may not be used. It should be also noted that since $\varepsilon_n^{\mathrm{mt}}$ is quantitatively equal to the volume change accompanying the transformation, it is not dependent on the martensite variant. $\mathbf{S}^{\alpha}$ is the unit second–order tensor which defines the direction of the shear associated with the α–variant of martensite and is defined as:

$$\mathbf{S}^{\alpha} = \mathbf{m}^{\alpha} \otimes \mathbf{n}^{\alpha} \tag{9}$$

where $\mathbf{m}^{\alpha}$ and $\mathbf{n}^{\alpha}$ are respectively the unit vector in the direction of transformation shear and the habit–plane unit normal, both associated with the α–variant of martensite.

In order to complete the description of the plastic flow rule given by Equation 7, one must define the evolution function for the volume fraction of each variant of martensite. In the present work the following power–law function is used:

$$\dot{f}^{\alpha} = \begin{cases} \dfrac{\dot{\gamma}_0}{\gamma^{\alpha-\mathrm{mt}}}\left(\dfrac{\tau^{\alpha} + \frac{\varepsilon_n^{\mathrm{mt}}}{\gamma^{\alpha-\mathrm{mt}}}\sigma_{\mathrm{h}}}{s^{\alpha}}\right)^{1/m} \\ 0 \end{cases}$$

$$\text{for } \left(\cdot\tau^{\alpha} + \frac{\varepsilon_n^{\mathrm{mt}}}{\gamma^{\alpha-\mathrm{mt}}}\sigma_{\mathrm{h}}\right) > 0 \text{ and } \sum_{\beta} f^{\beta} < 1 \tag{10a}$$

$$\text{for } \left(\cdot\tau^{\alpha} + \frac{\varepsilon_n^{\mathrm{mt}}}{\gamma^{\alpha-\mathrm{mt}}}\sigma_{\mathrm{h}}\right) \leq 0 \text{ or } \sum_{\beta} f^{\beta} \geq 1 \tag{10b}$$

$\dot{\gamma}_0$ and m in Equation 10a are model parameters (taken respectively as 0.001 s^{-1} and 0.01), τ^{α} the shear stress resolved in the habit plane (the plane of the martensitic plate face) in the direction of the transformation shear in the α–variant of martensite, σ_{h} the hydrostatic stress and s^{α} is the resistance of the parent phase toward transformation into the α–variant of martensite. Equation 10b is defined in order to take into account the fact that the martensitic transformation is irreversible and that it can take place as long as the parent phase is not completely transformed. The resolved shear stress and the hydrostatic stress are defined in the intermediate configuration in Fig. 1 as:

$$\tau^{\alpha} = \mathbf{T}^{*} \cdot \mathbf{S}^{\alpha} \tag{11a}$$

$$\sigma_{\mathrm{h}} = \left(\frac{1}{3}\right)\mathbf{T}^{*} \cdot \mathbf{I}. \tag{11b}$$

To complete the development of the constitutive model, one must also define an evolution equation for the transformation resistance s^{α}. Derivation of this equation is presented in Section 2.3. Once such an equation is defined, the evolution equation for the plastic deformation gradient, Equation 7, can be integrated to get $\mathbf{F}^{\mathrm{p}}$. Next, by solving Equation 1 for $\mathbf{F}^{*}$, combining it with Equation 5, and then with Equations 2–4 and 6 one obtains the Cauchy stress in the crystal. A detailed account of this procedure is given in the next section.

2.2. Integration procedure

Equation 7 can be integrated to yield:

$$\mathbf{F}^{\mathrm{p}}(\tau) = \exp[\Delta t\mathbf{L}^{\mathrm{p}}(\tau)]\mathbf{F}^{\mathrm{p}}(t) \tag{12}$$

where t and τ are respectively the time at the beginning and at the end of a time period Δt. Under the condition that Δt has a small magnitude, Equation 12 can be approximated as:

$$\mathbf{F}^{\mathrm{p}}(\tau) \approx [\mathbf{I} + \Delta t\mathbf{L}^{\mathrm{p}}(\tau)]\mathbf{F}^{\mathrm{p}}(t) \tag{13a}$$

or

$$\mathbf{F}^{\mathrm{p}-1}(\tau) \approx \mathbf{F}^{p-1}(t)[\mathbf{I} - \Delta t\mathbf{L}^{\mathrm{p}}(\tau)] \tag{13b}$$

where $\mathbf{L}^{\mathrm{p}}(\tau)$ is given by Equation 8 in which $\dot{f}^{\alpha}$ is replaced with $\dot{f}^{\alpha}(\tau)$.

If at the time τ, Equation 6 is substituted in Equation 4, $\mathbf{F}^{*\mathrm{T}}(\tau)$ and $\mathbf{F}^{*}(\tau)$ eliminated via Equation 1, and $\mathbf{F}^{\mathrm{p}}(\tau)$ and $\mathbf{F}^{\mathrm{p}-1}(\tau)$ respectively replaced using Equations 13a and 13b, one obtains the following relation:

$$\mathbf{T}^{*\mathrm{pt}}(\tau) \approx \mathbf{T}^{*\mathrm{tr}} - \sum_{\alpha} \Delta\gamma^{\alpha}(\tau)\mathbf{C}^{\alpha} \tag{14}$$

where $\mathbf{T}^{*\mathrm{tr}}$, $\Delta\gamma^{\alpha}$ and $\mathbf{C}^{\alpha}$ are define in Kalidindi [9]. $\mathbf{T}^{*\mathrm{tr}}$ and $\mathbf{C}^{\alpha}$ can be computed using the plastic deformation gradient at the beginning, $\mathbf{F}^{\mathrm{p}}(t)$, and the total deformation gradient at the end of a time interval, $\mathbf{F}(\tau)$. On other hand, $\Delta\gamma^{\alpha}(\tau)$ depend on $\mathbf{T}^{*\mathrm{pt}}(\tau)$ and hence Equation 14 represents a system of six nonlinear algebraic equations with six unknown components of $\mathbf{T}^{*}(\tau)$.

Once $\mathbf{T}^*(\tau)$ is determined by solving Equation 14, $\dot{f}^\alpha(\tau)$ is calculated via Equations 11a, 11b, 10a and 10b. Substituting $\dot{f}^\alpha(\tau)$ in Equations 8, 13a and next in (1) yields $\mathbf{F}^*(\tau)$. Finally, the Cauchy stress $\mathbf{T}^*(\tau)$ is determined by combining Equations 2–6.

2.3. Evolution equation for transformation resistance

To derive an evolution equation for transformation resistance, s^α, the grain shape is first idealized as a sphere and the martensite plate shape as an oblate spheroidal. Next, following Olson and Roitburd [11], the work of formation of a thin martensite plate is defined as:

$$\Delta W = \frac{4\pi}{3} r_\mathrm{p}^2 c_\mathrm{p} \Delta g + \frac{4\pi}{3} r_\mathrm{p} c_\mathrm{p}^2 K + 2\pi r_\mathrm{p}^2 \sigma_0 \qquad (15)$$

where r_p and c_p are respectively the radius and the semi–thickness of a martensite plate, Δg the free energy change accompanying martensitic transformation comprised of a chemical term (constant at a given temperature), a plate–shape independent strain–energy term, a parent–phase/martensite interface friction term and a term associated with the contribution of the activated nucleation site to martensite nucleation, K a plate shape–dependent strain energy parameter, and σ_0 the parent phase/martensitic surface energy. Within the isotropic elasticity framework, K is defined as $[\pi(2-\nu)/8(1-\nu)]\mu\gamma^{\mathrm{mt}} + [\pi/4(1-\nu)]\mu(\varepsilon_n^{\mathrm{mt}})^2$ where μ is the shear modulus and ν the Poisson's ratio.

To derive an expression for the evolution of transformation resistance, it is first recognized that a martensite plate initially forms as a very thin small plate and then grows in the radial direction at a very high speed (comparable with the speed of sound) until it encounters the parent–phase grain boundary at which point the radial plate growth ceases. Next, the plate continues to grow in the thickness direction at a substantially lower speed. The growth in the thickness direction ultimately becomes arrested since, according to Equation 15, as the plate thickens the work of transformation increases as c_p^2. The key assumption made in the present work is that s^α arises from the resistance the surrounding matrix exerts on a martensite plate as the thickness of the plate increase. The resistance the parent phase exerts on the martensite plate as the plate thickens can be defined as the rate of change of ΔW with the plate thickness per unit area of the parent phase/martensite plate interface, i.e.:

$$s^\alpha = \frac{1}{\pi\left(r_\mathrm{p}^\alpha\right)^2} \frac{\partial \Delta W^\alpha}{\partial c_\mathrm{p}^\alpha} = \frac{4}{3}\Delta g + \frac{8}{3} K^\alpha \frac{c_\mathrm{p}^\alpha}{r_\mathrm{p}^\alpha} \qquad (16)$$

The evolution equation for the transformation resistance s^α is obtained by differentiating Equation 16 with respect to time as:

$$\dot{s}^\alpha = \frac{8}{3} K^\alpha \frac{\dot{c}_\mathrm{p}^\alpha}{r_\mathrm{p}^\alpha\left(\sum_\beta f^\beta\right)} \qquad (17)$$

with the value of s^α at the instant of nucleation of martensite plate being:

$$s_0 = \frac{4}{3}\Delta g\left(\sum_\beta f^\beta\right). \qquad (18)$$

To account for the experimental observation that the martensite plates of progressively smaller size are formed as the transformation proceeds, the plate radius r_p in Equation 17 is made dependent on the total volume fraction of martensite at the instant when the plate is formed ($\sum_\beta f^\beta$). The value of the transformation resistance at the instant of nucleation of a martensite plate, s_0, is assumed in Equation 18 to be independent of the variant of martensite. However, to account for the fact that martensite nucleation is a heterogeneous process and that it is controlled by the preexisting nucleation sites, and that as the transformation proceeds new martensite plates are formed by the activation of nuclei of progressively lower potency, s_0 is made dependent on the total volume fraction of martensite at the instant of plate nucleation, $\sum_\beta f^\beta$.

Under the assumption that at any time during transformation only one plate of martensite of the α–variant grows within each parent–phase grain, the rate of increase of the martensite plate thickness $\dot{c}_\mathrm{p}^\alpha$, can be expressed as a function of the rate of increase of the volume fraction of the α–variant of martensite using the following procedure:

First, the ratio of the volumes of a single martensite plate of the α–variant and the (untransformed) parent–phase grain is given as:

$$f^\alpha = \frac{\left[(4/3)\pi\left(r_\mathrm{p}^\alpha\right)^2 c_\mathrm{p}^\alpha\right]}{\left[(4/3)\pi r_\mathrm{g}^3\right]} \qquad (19)$$

where r_g is the grain radius. Differentiation of Equation 19 with respect to time yields:

$$\dot{f}^\alpha = \frac{\left[r_\mathrm{p}^\alpha\left(\sum_\beta f^\beta\right)\right]^2}{r_\mathrm{g}^3} \dot{c}_\mathrm{p}^\alpha. \qquad (20)$$

Substitution of Equation 20 into Equation 17 yields:

$$\dot{s}^\alpha = \frac{8}{3} K^\alpha \left[\frac{r_\mathrm{g}}{r_\mathrm{p}\left(\sum_\beta f^\beta\right)}\right]^3 \dot{f}^\alpha. \qquad (21)$$

The superscript α is dropped from r_p in Equation 21 since, in general, the change of the martensite plate size with the extent of transformation is not dependent on the martensite variant. The term within the brackets on the right-hand side of Equation 21 can be determined using experimental data pertaining to the change of the average volume of the martensite plate $\overline{v}_\mathrm{p}$ and the plate aspect ratio $c_\mathrm{p}/r_\mathrm{p}$ with the total volume fraction transformed, $\sum_\beta f^\beta$, using the following procedure.

First, one can readily derive the following relation between the instantaneous plate volume v_p and the average plate volume:

$$v_{\mathrm{p}}\left(\sum_{\beta} f^{\beta}\right) = \overline{v}\left(\sum_{\beta} f^{\beta}\right) + \sum_{\beta} f^{\beta} \frac{\mathrm{d}\left[\overline{v}_{\mathrm{p}}\left(\sum_{\beta} f^{\beta}\right)\right]}{\mathrm{d}\left(\sum_{\beta} f^{\beta}\right)}. \quad (22)$$

Next, the expression for the ratio of the instantaneous plate volume and the volume of a parent–phase grain, v_{g}, can be rearranged as:

$$\frac{v_{\mathrm{p}}\left(\sum_{\beta} f^{\beta}\right)}{v_{\mathrm{g}}} = \frac{r_{\mathrm{p}}^2\left(\sum_{\beta} f^{\beta}\right) c_{\mathrm{p}}}{r_{\mathrm{g}}^2} = \left[\frac{r_{\mathrm{p}}\left(\sum_{\beta} f^{\beta}\right)}{r_{\mathrm{g}}}\right]^3 \left[\frac{c_{\mathrm{p}}}{r_{\mathrm{p}}}\left(\sum_{\beta} f^{\beta}\right)\right]. \quad (23)$$

Equation 23 can be solved for the first term on the right-hand side in terms of the left-hand side of this equation and then substituted in Equation 21.

To determine the Δg vs. $\sum_{\beta} f^{\beta}$ relation, the statistical model of martensite nucleation originally developed by Olson *et al.* [1] has been used. According to this model, the potency of a nucleation site, expressed in terms of a defect size parameter, n, is defined as a following function of Δg:

$$n = \frac{2\sigma_0}{\varrho V_{\mathrm{m}} \Delta g} \quad (24)$$

where ϱ is the surface atomic density for the parent phase/martensite interface and V_{m} the molar volume. Nucleation sites of the highest potency are activated first and as the martensitic transformation proceeds the sites of progressively lower potency are activated. This relation between n and $\sum_{\beta} f^{\beta}$ is expressed by Chen *et al.* [12] as:

$$n = -\frac{1}{\alpha} \ln\left(\sum_{\beta} f^{\beta}\right) \quad (25)$$

where α is a site–potency distribution parameter.

By combining Equation 24 and 25 and by including a term corresponding to the magnitude of the Gibbs free energy change at M_{s}, Δg_0, one obtains:

$$\Delta g\left(\sum_{\beta} f^{\beta}\right) = \frac{\Delta g_0}{V_{\mathrm{m}}} - \frac{2\alpha\sigma_0}{\varrho V_{\mathrm{m}} \ln\left(\sum_{\beta} f^{\beta}\right)}. \quad (26)$$

Equation 26 shows that as the martensitic transformation approaches completion ($\sum_{\beta} f^{\beta} \to 1$), Δg (and hence the deformation resistance at the instant of plate formation) becomes infinitely large. This finding is consistent with numerous experimental observations which show that fracture occurs before the stress–assisted martensitic transformation is complete.

3. Application of the model to the b.c.c.→f.c.o. martensite transformation in Ti–10V–2Fe–3Al (wt.%)

The crystal plasticity model developed in the previous section is next implemented in a finite element program to analyze the stress–assisted b.c.c.→f.c.o. martensitic transformation in Ti–10V–2Fe–3Al (wt.%), the alloy which was studied experimentally by Duerig *et al.* [13].

3.1. Crystallography of b.c.c.→f.c.o. martensitic transformation

To determine the basic crystallographic data associated with the b.c.c.→f.c.o. martensitic transformation in the Ti–10V–2Fe–3Al alloy, the CRAB theory originally proposed by Crocker [14] is utilized. A brief overview of the CRAB theory is given in Appendix A.

The main assumption incorporated in the CRAB theory is that the overall strain accompanying the formation of a martensite plate is an invariant plane strain (IPS) with the plate faces being the invariant planes. In addition to a strain associated with the change in the crystal structure accompanying the martensitic transformation, the Bain strain and a lattice rotation, a shear–type deformation (twinning in the case of the Ti–10V–2Fe–3Al alloy) which leaves the crystal structure of martensite unaltered, the lattice invariant deformation, also takes place. The necessary input parameters for the CRAB theory used in the present work are given in Table I.

In accordance with the experimental results of Williams [15], the lattice invariant deformation is adopted to take place by twinning on $\{111\}_{\mathrm{f.c.o.}} \Leftrightarrow \{110\}_{\mathrm{b.c.c.}}$ planes. Following the procedure of Bowles

TABLE I Input parameters used in the calculations of the crystallographic parameters associated with the martensitic transformation in Ti–10V–2Fe–3Al (wt.%)

Lattice Parameters, $\mathring{A}$	$a_{\mathrm{b.c.c.}} = 3.2275$; $a_{\mathrm{f.c.o.}} = 3.01$, $b_{\mathrm{f.c.o.}} = 4.83$, $c_{\mathrm{f.c.o.}} = 4.62$
Transformation Volume Change	$\varepsilon_n^{\mathrm{mt}} = 1 - \det(\boldsymbol{G}) = .001089$
Lattice Correspondence	$[1\,0\,0]_{\mathrm{b.c.c.}} \Leftrightarrow \langle 1\,0\,0\rangle_{\mathrm{f.c.o.}}$ $[0\,1\,0]_{\mathrm{b.c.c.}} \Leftrightarrow \langle 0\ .5\ .5\rangle_{\mathrm{f.c.o.}}$ $[0\,0\,1]_{\mathrm{b.c.c.}} \Leftrightarrow \langle 0\ \overline{.5}\ .5\rangle_{\mathrm{f.c.o.}}$
Lattice Invariant (Twinning) Plane Normal	$\mathbf{o} = \begin{pmatrix} .707107 \\ .707107 \\ 0 \end{pmatrix}_{\mathrm{bcc}}; \begin{pmatrix} -.707107 \\ .707107 \\ 0 \end{pmatrix}_{\mathrm{bcc}}; \begin{pmatrix} .707107 \\ 0 \\ .707107 \end{pmatrix}_{\mathrm{bcc}}; \begin{pmatrix} -.707107 \\ 0 \\ .707107 \end{pmatrix}_{\mathrm{bcc}}$
Lattice Invariant (Twinning) Direction	$\mathbf{l} = \begin{bmatrix} .682173 \\ -.682173 \\ 263213 \end{bmatrix}_{\mathrm{bcc}}; \begin{bmatrix} -.682173 \\ -.682173 \\ 263213 \end{bmatrix}_{\mathrm{bcc}}; \begin{bmatrix} .682173 \\ 263213 \\ -.682173 \end{bmatrix}_{\mathrm{bcc}}; \begin{bmatrix} -.682173 \\ 263213 \\ -.682173 \end{bmatrix}_{\mathrm{bcc}}$
Twinning Magnitude	$\gamma^{\mathrm{tw}} = .214035$

TABLE II Crystallographic data for the b.c.c.→f.c.o. martensitic transformation in Ti–10V–2Fe–3Al (wt.%) associated with the $[100]_{\text{b.c.c.}} \Leftrightarrow [100]_{\text{f.c.o.}}$, $[010]_{\text{b.c.c.}} \Leftrightarrow [0.5.5]_{\text{f.c.o.}}$, $[001]_{\text{b.c.c.}} \Leftrightarrow [0\,\overline{.5}\,.5]_{\text{f.c.o.}}$ lattice correspondence and $[.707107.707107\,0]_{\text{b.c.c.}}(.682173 - .682173.263213)_{\text{b.c.c.}}$ lattice invariant shear (LIS): IPS – invariant phase strain, see Appendix A for details

Variant Number	IPS Plane Normal **n**	IPS Direction **u**	IPS Magnitude g	IPS Shear Direction **m**	IPS Shear Magnitude γ^{mt}	LIS Magnitude v
1	$\begin{bmatrix} .744870 \\ -.306356 \\ .592552 \end{bmatrix}$	$\begin{bmatrix} -.676145 \\ -.315933 \\ .665743 \end{bmatrix}$	.0880013	$\begin{bmatrix} -.058691 \\ -.028136 \\ .059231 \end{bmatrix}$	.088003	.053026
2	$\begin{bmatrix} .643119 \\ .329285 \\ -.691546 \end{bmatrix}$	$\begin{bmatrix} .773458 \\ .329285 \\ -.691546 \end{bmatrix}$		$\begin{bmatrix} -.067364 \\ .026054 \\ -.050242 \end{bmatrix}$	.087983	
3	$\begin{bmatrix} .306382 \\ -.744944 \\ .592598 \end{bmatrix}$	$\begin{bmatrix} .315895 \\ .676083 \\ .665691 \end{bmatrix}$	.0880010	$\begin{bmatrix} .028133 \\ .058685 \\ .059227 \end{bmatrix}$	.087995	.161009
4	$\begin{bmatrix} .329237 \\ .643033 \\ .691472 \end{bmatrix}$	$\begin{bmatrix} .292025 \\ -.773553 \\ .562424 \end{bmatrix}$		$\begin{bmatrix} .026057 \\ -.067373 \\ -.050247 \end{bmatrix}$	.087994	

and Mckenzie [16], the twinning direction and its magnitude are determined, Table I. The CRAB theory yielded 48 variants of martensite. Four of these 48 variants corresponding to the $[100]_{\text{b.c.c.}} \Leftrightarrow [100]_{\text{f.c.o.}}$, $[010]_{\text{b.c.c.}} \Leftrightarrow [0\,.5\,.5]_{\text{f.c.o.}}$, $[001]_{\text{b.c.c.}} \Leftrightarrow [0\,\overline{.5}\,.5]_{\text{f.c.o.}}$ lattice correspondence and the $[.707107.7071070]_{\text{b.c.c.}}$ $(.682173{-}.682173.263213)_{\text{b.c.c.}}$ lattice invariant (twinning) shear are given in Table II.

3.2. Evolution equation for transformation resistance

Using quantitative metallography and image analysis of partially transformed Ti–10V–2Fe–3Al, the following relations for the change in the martensite plate volume and the plate aspect ratio have been obtained in our ongoing work [17]:

$$\overline{v}_{\text{p}}\left(\sum_{\beta} f^{\beta}\right) = \frac{4.5 \times 10^3}{\sum_{\beta} f^{\beta} + 0.09}(\mu\text{m}^3) \qquad (27)$$

and

$$\frac{c_{\text{p}}}{r_{\text{p}}}\left(\sum_{\beta} f^{\beta}\right) = 0.2 - \frac{0.01}{\sum_{\beta} f^{\beta} + 0.08} \qquad (28)$$

Equations 27 and 28 are used to construct the evolution equation for the transformation resistance, Equation 21.

The remaining model parameters for the Ti–10V–2Fe–3Al alloy are summarized in Table III.

TABLE III Values of the material parameters for Ti–10V–2Fe–3Al (wt.%) used in the implementation of the constitutive model

Parameter	Unit	Value	Reference
μ	GPa	58.0	[7, 8]
ν	No unit	0.3	[7, 8]
α	No unit	0.84	[7, 8]
σ_0	J/m^2	0.35	[7, 8]
ϱ	mol/m^2	3.01×10^{-5}	[7, 8]
V_{m}	m^3/mol	8.98×10^{-6}	[7, 8]
Δg_0	J/mol	700	[7, 8]

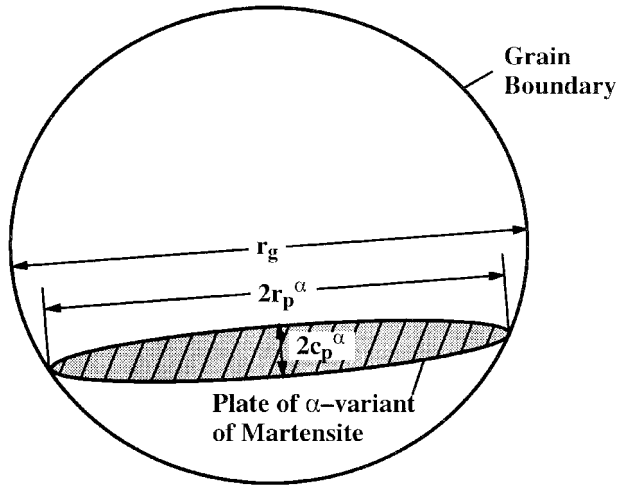

Figure 2 A schematic of a circular parent–phase grain of radius r_{g} containing an oblate–spheroidal martensite plate of radius r_{p}^{α} and semi–thickness c_{p}^{α}.

3.3. Finite element simulation of stress–assisted martensitic transformation under different stress and strain states

To determine the effect of stress and strain states on the evolution of martensite and the shape of the corresponding equivalent stress–equivalent strain curve, finite element simulations of uniaxial and plane–strain compression and bi–axial tension of the polycrystalline Ti–10V–2Fe–3Al alloy are carried out. In each case, a finite element mesh consisting of 343 eight–node three–dimensional elements (ABAQUS designation C3D8) is used. The initial mesh is shown in Fig. 3a. Each element is taken to represent a grain (a single crystal) and the initial orientation of each element is set at random. In the case of uniaxial compression, the top and the bottom faces of the finite–element mesh are constrained to remain planar during deformation, made free of shear tractions and subject to displacement boundary conditions consistent with a true axial strain rate of –0.001 s^{-1}. In the case of plane–strain compression, the same boundary conditions are applied to the top and to the bottom of the mesh as in the case of uniaxial compression. In addition, however, no strain normal to the

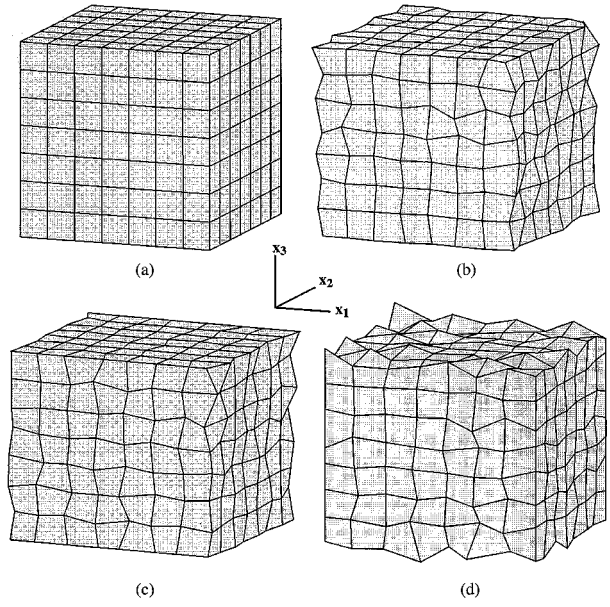

Figure 3 Initial finite element mesh containing 343 eight–node three–dimensional elements: (a) initial mesh, (b) mesh after uniaxial compression, (c) mesh after plane–strain compression and (d) mesh after bi–axial tension. Meshes in (b)–(d) correspond to the equivalent plastic strain of 0.05.

front and the back faces of the mesh are allowed. In the case of bi–axial tension, no constraints are imposed on the top and the bottom faces of the mesh. However, the left/right and front/back faces are constrained to remain planar and subject to displacement boundary conditions consistent with a normal strain rate of 0.0005 s^{-1}. Deformed meshes corresponding to the equivalent strain of 0.05 obtained under uniaxial compression, plane–strain compression and bi–axial tension are shown in Fig. 3b–d, respectively.

To carry out a finite element analysis of the stress–assisted martensitic transformation, the crystal–plasticity materials constitutive model and the material state integration procedure, developed respectively in Sections 2.1 and 2.2, are implemented in ABAQUS Standard finite element program [18]. Specifically, the model is implemented in a User Material Subroutine (UMAT) within which the Cauchy stress and all the state variables (the deformation resistance and the volume fraction of each martensite variant) are updated for the prescribed total deformation gradient at the end of a time step. In addition, the material Jacobian is computed within UMAT using a finite difference perturbation procedure [9]. The material Jacobian is required in the global Newton scheme of ABAQUS/Standard in order to achieve an accurate assessment of the kinematics.

In order to simplify the calculations and reduce the computational time, only 12 out of 48 variants of martensite are considered in the present work. The 12 variants are chosen in such a way that if two or more variants have comparable orientations of their habit plane and/or direction of shear only one is retained in the analysis. In addition, only one variant of martensite is allowed to be operational within a given grain at any time step. This was done in order to mimic the actual mechanism of martensitic transformation in which individual plates are formed within a grain at different times, and a new plate is generally formed only after the plate which was operational in the last time increment, stops growing. This procedure allows the prediction of the evolution of the average martensite plate volume with the progress of martensitic transformation. That is, if the same martensite variant is found to be operational over a number of consecutive time increments within a given grain, it is assumed that within this time period the transformation within that grain occurs by the nucleation and growth of the same martensite plate. The variant of martensite which is operational within each time increment is defined as the one which is characterized by a maximum rate of increase of the martensite volume fraction, $\dot{f}^{\alpha}$.

To verify texture development during the stress–assisted martensitic transformation under the three deformation modes discussed earlier, the orientation of a specific set of crystallographic planes and directions in all martensite variants at all integration points of each grain is determined in the current configuration. This is done by applying the following transformation operation to the crystal plane normal $\mathbf{n}_{\mathrm{cp}} = \{110\}_{\mathrm{b.c.c.}}$ and the crystallographic direction $\mathbf{m}_{\mathrm{cp}} = \langle 111\rangle_{\mathrm{b.c.c.}}$ in the parent phase which correspond to a close–packed plane and close–packed direction in martensite:

$$\mathbf{n}^{\alpha}_{\mathrm{cp}} = \frac{\mathbf{F}^{*-\mathrm{T}}(\tau)\mathbf{R}^{\alpha}\mathbf{P}^{\alpha-1}\mathbf{n}_{\mathrm{cp}}}{[\det(\mathbf{F}^{*-\mathrm{T}})\det(\mathbf{P}^{\alpha-1})]} \tag{29}$$

and:

$$\mathbf{m}^{\alpha}_{\mathrm{cp}}(\tau) = \frac{\mathbf{F}^{*-\mathrm{T}}(\tau)\mathbf{R}^{\alpha}\mathbf{P}^{\alpha}\mathbf{m}_{\mathrm{cp}}}{[\det(\mathbf{F}^{*-\mathrm{T}})\det(\mathbf{P}^{\alpha})]} \tag{30}$$

for the α–variant of martensite. Next, the corresponding (equal–area projection) pole figures are generated by using the volume fractions of martensite variants to weigh their contributions to the "signal" intensity. This was done by identifying in each grain the three variants of martensite which have the largest volume fraction. The volume fractions of these variants are prorated so that their sum becomes equal to 1.0. The (0,1) range is next divided in five segments each 0.2 wide and each segment numbered as: segment 1, 0–0.2; segment 2, 0.2–0.4; etc. Next, the prorated volume fractions of the three variants are assigned a number consistent with a corresponding segment number. For example, if the volume fraction of one of the variants is 0.35, that variant is assigned a number 2. The numbers assigned represent the number of closely spaced + symbols used to represent the contribution of the variant in question to the pole figure.

A comparison between the computed and the experimental [13] uniaxial compression equivalent stress–equivalent strain curves for Ti–10V–2Fe–3Al are shown in Fig. 4. Following the procedure of Grujicic and Sankaran [7], the original experimental data were revised to remove the effect of 10 vol.% of a second phase. Based on the results shown in Fig. 4, the model developed here seems to account reasonably well for the experimentally observed equivalent stress–equivalent

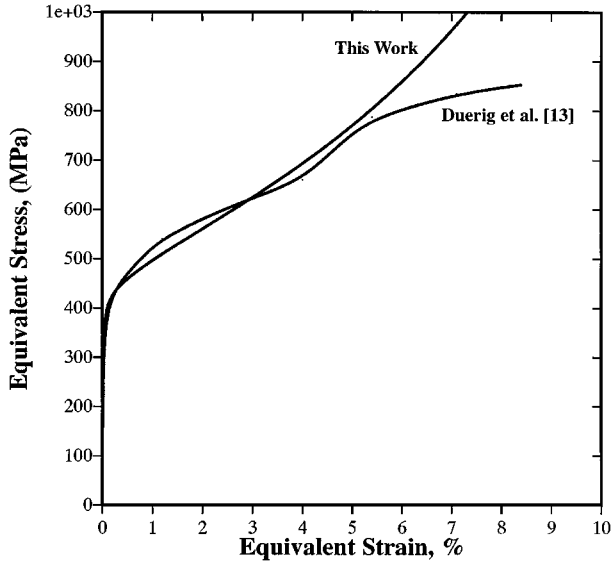

Figure 4 A comparison of the equivalent stress–equivalent strain curve for uniaxial compression predicted by the model with the experimental results of Duerig *et al.* [13].

strain relationship in the early stages of deformation including the stage when the material displays a normal decreasing rate of strain hardening and when the material begins to develop an unusual increasing rate of strain hardening. However, at the later stages of deformation the two equivalent stress–equivalent strain curves begin to diverge. This can be readily understood since the proposed model considers the stress–assisted martensitic transformation as a sole mechanism of inelastic deformation. Therefore, at the later stages of deformation, martensitic transformation proceeds by the activation of martensite nuclei of low potency. Consequently, the (calculated) equivalent stress needed to the maintain martensitic transformation continues to increase with the equivalent strain. In the actual material, on the other hand, slip and/or twinning in the parent phase are available as potential mechanisms for inelastic deformation. Consequently, when the stress required to maintain the operation of martensitic transformation becomes too high, slip and/or twinning take over as the dominant modes of inelastic deformation. As a result, one observes a normal "parabolic–type" hardening characterized by a decreasing rate of strain hardening in the later stages of inelastic deformation.

The equivalent stress–equivalent strain curves and the martensite volume fraction–equivalent strain curves for the three deformation modes discussed above are shown in Fig. 5a and b, respectively. The results shown in these figures can be summarized as following:

– For each mode of deformation, a normal strain–hardening behavior characterized by a decreasing rate of stain hardening is observed at low values of the equivalent strains. This behavior is generally attributed to the combined effects of strain hardening and lattice rotation accompanying the inelastic deformation.

– At the later stages of deformation, an unusual "upward" hardening characterized by an increase in the rate of strain hardening with the equivalent strain is observed. This finding is consistent with the fact that as the transformation proceeds, nucleation sites of a progressively lower potency (a higher initial transformation resistance, Equation 26) are activated.

– The equivalent stress–equivalent strain curve is significantly affected by the mode of deformation. Specifically, higher equivalent stress values are observed in the cases of plane–strain compression and bi–axial tension in comparison to the one found in the case of uniaxial compression. This finding is consistent with the fact that, since the transformation volume change is negative in Ti–10V–2Fe–3Al, a positive (tensile) hydrostatic stress opposes while a negative (compressive) hydrostatic stress assists the martensitic transformation. Therefore, lowest levels of the equivalent stress are seen in the case of uniaxial compression where the hydrostatic stress is most negative.

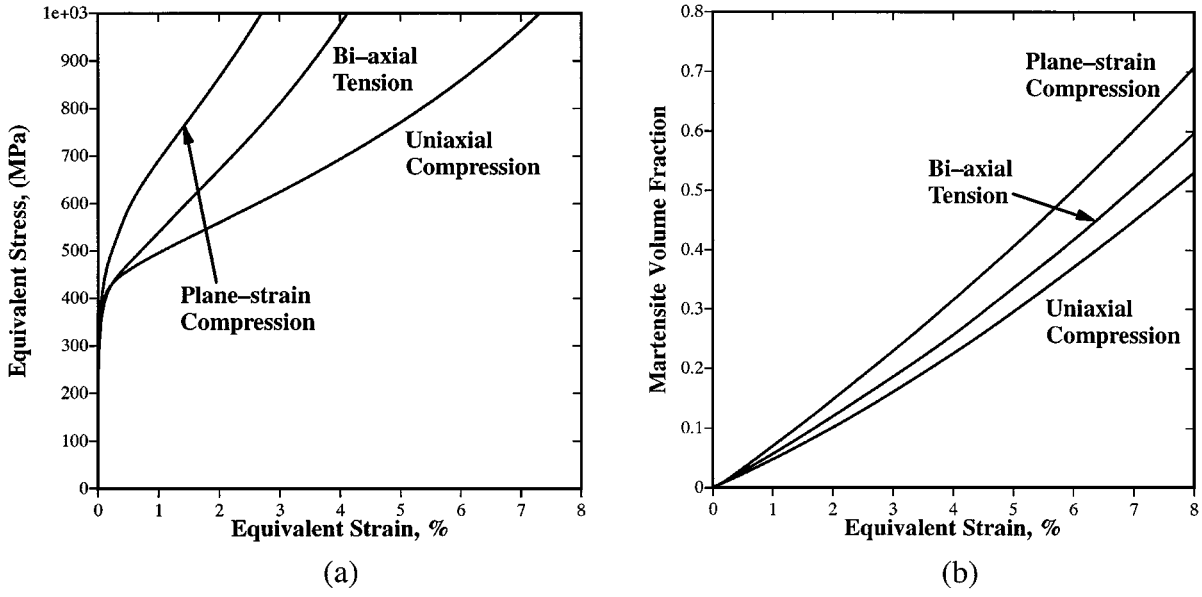

Figure 5 Effect of deformation mode on the equivalent stress–equivalent strain and volume fraction of martensite–equivalent strain curves as predicted by the model.

– For each of the three modes of deformation there is a monotonic, approximately linear increase in the volume fraction of martensite with the equivalent plastic strain, Fig. 5b. This finding is consistent with the fact that the martensitic transformation is the sole mode of inelastic deformation considered and that the transformation is irreversible.

– The extent of martensitic transformation at a given level of the equivalent strain is dependent on the deformation mode, Fig. 5b. This dependence is, however, significantly weaker than the equivalent strain dependence of the equivalent stress, Fig. 5a. Nevertheless, the relative position of the three curves in Fig. 5a and b is identical (i.e. the curves corresponding to uniaxial compression are at the bottom, etc.). This finding suggests that the highest level of stress biasing of the martensitic transformation is achieved in the case of uniaxial compression.

– The cases of uniaxial compression and bi–axial tension can be considered as ones in which the strain state of the entire computational domain are very similar at a given level of the equivalent strain. Hence, the observed differences in the equivalent stress–equivalent strain curves and the martensite volume fraction–equivalent strain curves can be attributed almost exclusively to the effect of stress state (more specifically to the effect of the hydrostatic stress).

– The equivalent stress–equivalent strain and the volume fraction of martensite–equivalent strain curves for plane–strain compression lie generally above the ones for uniaxial compression and bi–axial tension. If the sign and the magnitude of the hydrostatic stress were the only factors affecting the progress of martensitic transformation, one should expect these curves for plane–strain compression (moderate negative hydrostatic stress) to be located between the corresponding curves for uniaxial compression (large negative–hydrostatic stress) and bi–axial tension (positive hydrostatic stress). Since this conjecture is not supported by the experimental results, it appears that the strain state (different in plane–strain compression relative to uniaxial compression and bi–axial tension) also has an important effect on the progress of martensitic transformation.

The (equal–area projection) $(110)_{b.c.c.}$–type pole figures for the initial 343–grain polycrystalline material are shown in Fig. 6. The corresponding (equal–area projection) $(111)_{f.c.o.}$–type pole figures at the equivalent strain of 0.05 in the partially transformed Ti–10V–2Fe–3Al under uniaxial compression, plane–strain compression and bi–axial tension are shown in Figs 7–9, respectively. While no experimental data are currently available to help establish the validity of the computed pole figures, it should be noted that the texture obtained in uniaxial compression and bi–axial tension are very similar to each other and substantially different from the texture obtained in plane–strain compression. This finding is consistent with our previous observation that uniaxial compression and bi–axial tension result in similar macroscopic strain states. It should be also noted that for easier comparison with their experimental counterpart the discrete grain pole figures shown in Figs 6–9 should be transformed into probability density plots. This could be done using DIOR program contained in the popLA software package [19].

The effect of the extent of martensitic transformation on the average volume of the martensite plate in Ti–10V–2Fe–3Al undergoing the b.c.c.→f.c.o. stress–assisted martensitic transformation in uniaxial compression is shown, as a band, in Fig. 10. The solid curve shown in the same figure corresponding to the experimentally observed relationship, Equation 32. The results shown in Fig. 10 indicate a fair agreement between the predicted and the measured results. Similar average martensite plate volume–equivalent strain bands are obtained for the other two modes of deformation and hence are not shown.

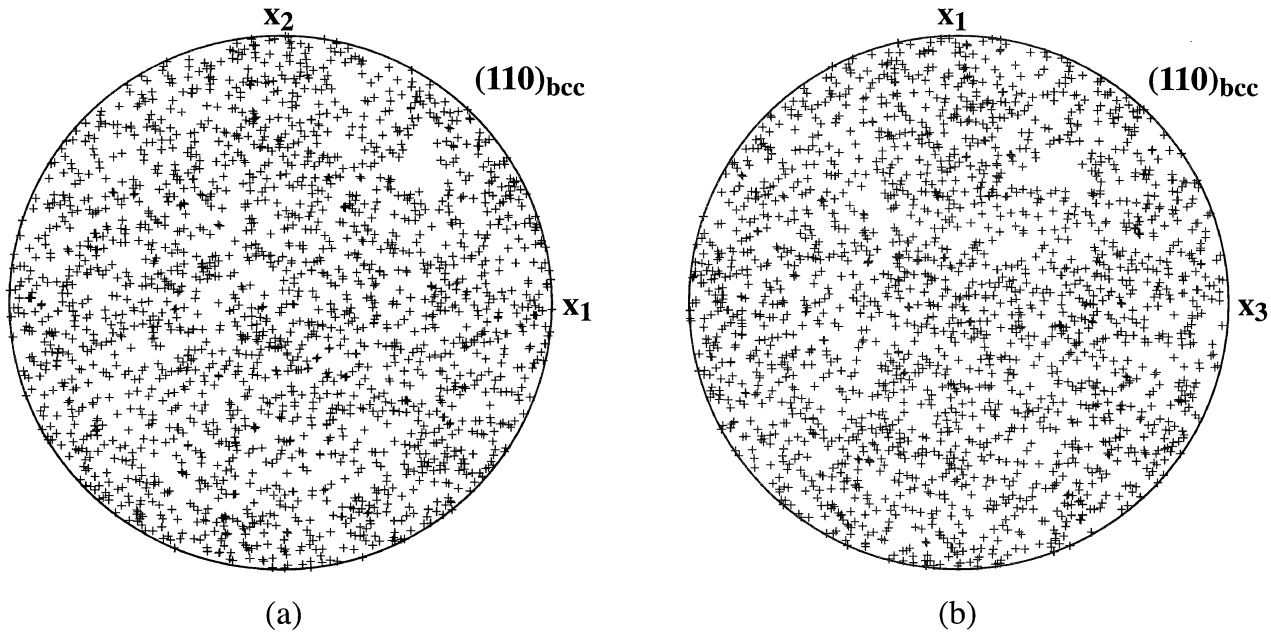

Figure 6 $\{111\}_{b.c.c.}$ (equal area projection) pole figures showing the initial "isotropic" texture in the 343–grain polycrystal.

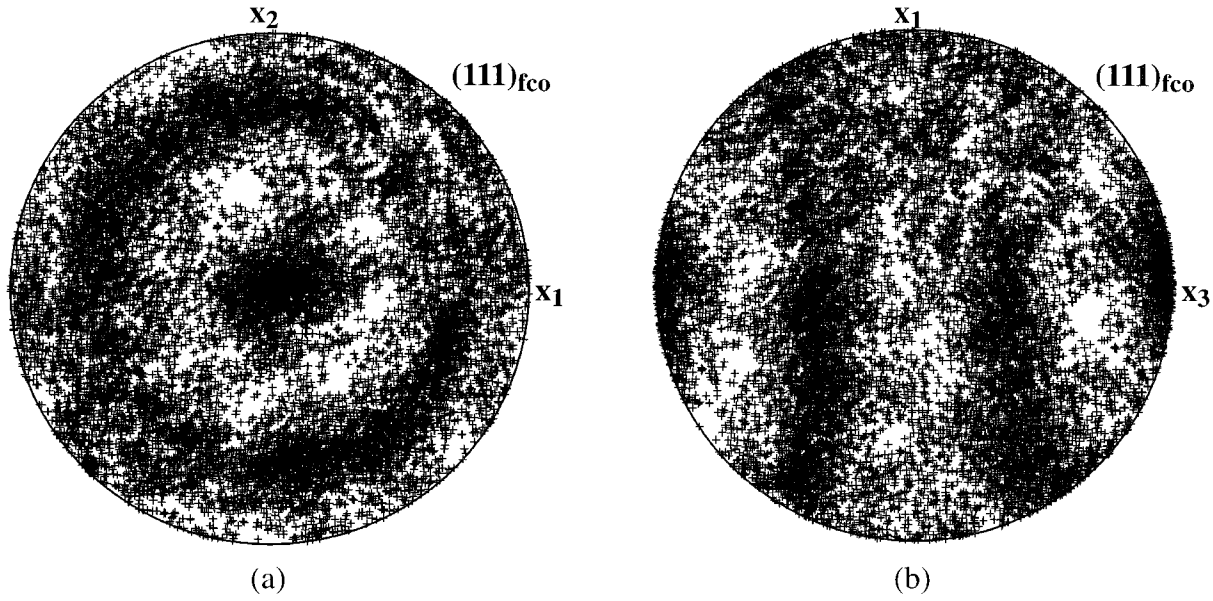

Figure 7 $\{111\}_{\text{f.c.o.}}$ (equal area projection) pole figures for the partially–transformed Ti–10V–2Fe–3Al deformed to an equivalent strain level of $\bar{\epsilon} = 0.05$ in uniaxial compression.

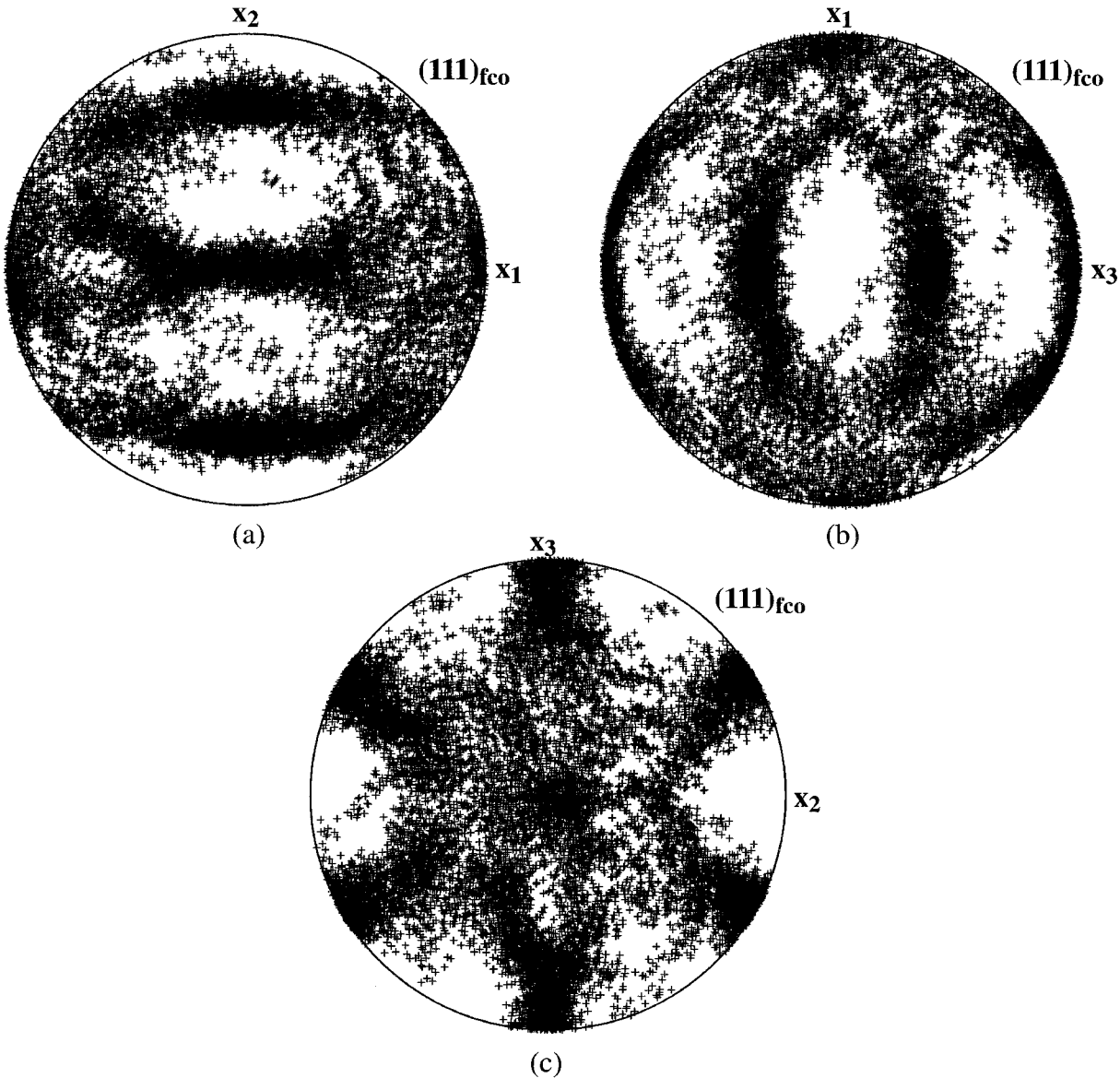

Figure 8 $\{111\}_{\text{f.c.o.}}$ (equal area projection) pole figures for the partially–transformed Ti–10V–2Fe–3Al deformed to an equivalent strain level of $\bar{\epsilon} = 0.05$ in plane–strain compression.

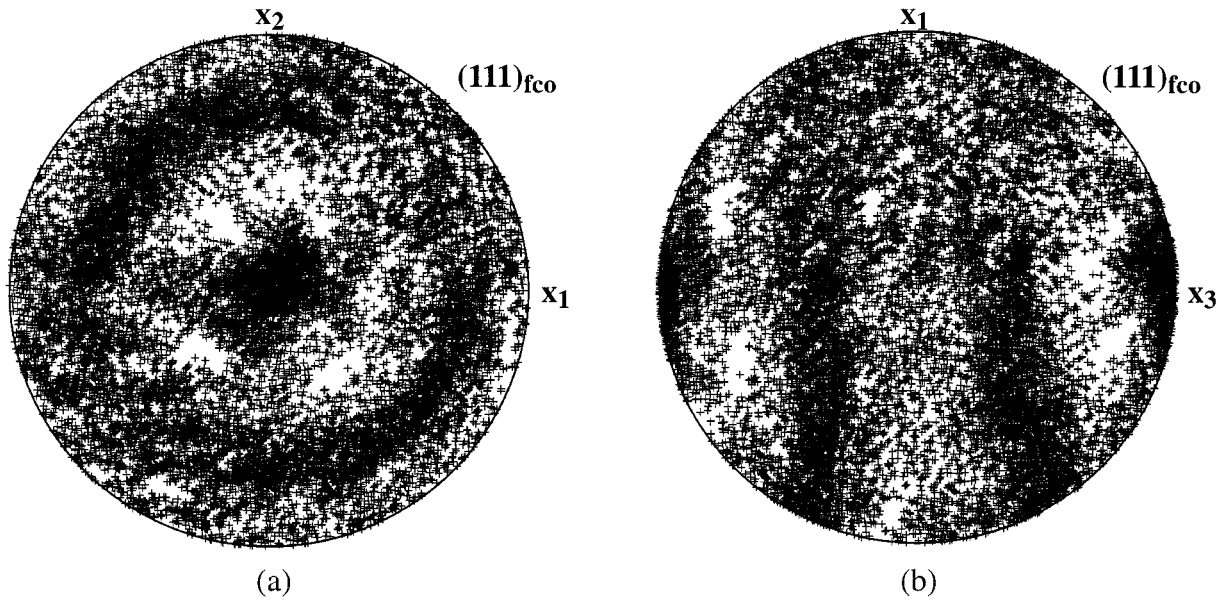

Figure 9 $\{111\}_{\text{f.c.o.}}$ (equal area projection) pole figures for the partially–transformed Ti–10V–2Fe–3Al deformed to an equivalent strain level of $\bar{\epsilon} = 0.05$ in bi–axial tension.

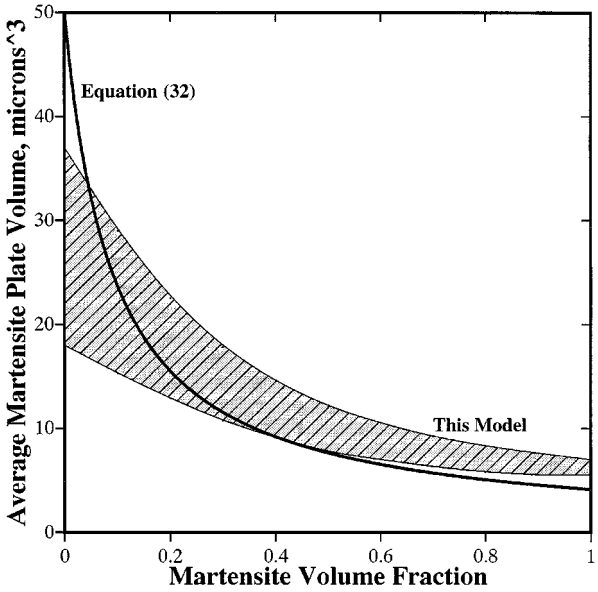

Figure 10 Effect of the extent of martensitic transformation on the average volume of the martensite plate.

4. Conclusions

Based on the results obtained in the present work the following conclusions can be drawn.

– By combining the basic theories for crystallography, thermodynamics, kinetics and statistics of martensitic transformation with the theory of crystal plasticity, a materials constitutive model for the stress–assisted martensitic transformation suitable for implementation in a finite element formulation can be developed.

– While more experimental data are needed to validate the model, preliminary results suggest that the model can reasonably well account for the measured uniaxial–compression equivalent stress–equivalent strain relation associated with the stress–assisted martensitic transformation in Ti–10V–2Fe–3Al.

– The model suggests that the evolution of martensite and the corresponding equivalent stress–equivalent strain curves are affected both by the applied stress state (primarily the sign and the magnitude of the hydrostatic stress) and by the strain state.

– The stress–assisted martensitic transformation in Ti–10V–2Fe–3Al results in the formation of the texture in the transformed materials. The nature of the texture appears to be mainly controlled by the imposed macroscopic strain state.

– The proposed model correctly predicts the experimentally measured decrease of the average martensite plate volume with the extent of transformation.

Appendix A: Single lattice–invariant shear CRAB theory of martensite crystallography

The overall deformation accompanying martensitic transformation of parent phase into a single variant of martensite is defiend as an invariant plane strain (IPS) **G** of magnitude g on a plane with a unit normal **n** in a unit direction **u**:

$$\mathbf{G} = \mathbf{I} + g\mathbf{u} \otimes \mathbf{n}. \tag{A1}$$

G can be multiplicatively decomposed in a lattice rotation **R**, a (symmetric) lattice strain **P** and a lattice invariant shear **V** as:

$$\mathbf{G} = \mathbf{RPV}. \tag{A2}$$

R can be eliminated from Equation A2 using the identity, $\mathbf{R}^{\mathrm{T}}\mathbf{R} = \mathbf{I}$, to yield:

$$\mathbf{G}^{\mathrm{T}}\mathbf{G} = \mathbf{V}^{\mathrm{T}}\mathbf{P}^2\mathbf{V} = \mathbf{Q} \tag{A3}$$

or

$$\mathbf{X} = \mathbf{G}^{\mathrm{T}}\mathbf{G} - \mathbf{Q} = \mathbf{0}. \tag{A4}$$

Since **X** is symmetric, substitution of Equation A1 in Equation A4 yields six algebraic equations in the form:

$$X_{ii} = g^2 n_i^2 + 2g u_i n_i + 1 - Q_{ii} = 0 \tag{A5a}$$

and

$$X_{ij} = g^2 n_i n_j + g(u_i n_j + u_j n_i) - Q_{ij} = 0 \quad (i \neq j). \tag{A5b}$$

where $i, j = 1, 2, 3$.

Equations A5a and A5b can be solved in the following way for the five unknowns g, n_1/n_3, n_2/n_3, u_1/u_3 and u_2/u_3, a single unknown parameter (the magnitude of the lattice invariant shear, v) contained in **Q**. First, substitution of Equation A5a in the trace $X_{11} + X_{22} + X_{33}$ of **X** gives:

$$g^2 = Q_{11} + Q_{22} + Q_{33} - 2(\det \mathbf{G}) - 1, \tag{A6}$$

where $\det \mathbf{G} = 1 - \varepsilon_n^{\mathrm{mt}}$ is numerically equal to the ratio of the volumes of the corresponding cells of martensite and the parent phase. Equation A6 yields two values of g equal in magnitude and opposite in sign. Next, if Equations A5a and A5b are substituted into the expression $2n_i n_j X_{ij} - n_j^2 X_{ii} - n_i^2 X_{jj} = 0$, one obtains the following three quadratic equations:

$$(1 - Q_{ii})n_j^2 + 2Q_{ij}n_i n_j + (1 - Q_{jj})n_i^2 = 0 \quad (1 \neq j = 1, 2, 3). \tag{A7}$$

In general, Equations A7 yields two solutions for the invariant plane strain unit normal **n**. Inspection of Equation A5a shows that there is one IPS direction **u** for each $g/\mathbf{n}$ pair and that changing the sign of g simply changes the sign of **u** and, hence, does not yield a distinct solution. Thus, for each **Q** Equations A5, A6 and A7 yield two solutions for the invariant plane strain **G**.

Q can be determined by first inverting Equation A3 to obtain:

$$\mathbf{G}^{-1}\mathbf{G}^{\mathrm{T}-1} = \mathbf{V}^{-1}\mathbf{P}^{-1}\mathbf{P}^{\mathrm{T}-1}\mathbf{V}^{\mathrm{T}-1} = \mathbf{Q}^{-1} \tag{A8}$$

If Equation A1 is inverted to yield:

$$\mathbf{G}^{-1} = \mathbf{I} - g(\det \mathbf{G})^{-1}\mathbf{u} \otimes \mathbf{n} \tag{A9}$$

and Equation A9 plugged in Equation A8 one obtains:

$$\overline{X}_{ii} = (\det \mathbf{G})^{-2} g^2 u_i^2 - 2(\det \mathbf{G})^{-1} g n_i u_i + 1 - Q_{ii}^{-1} = 0 \quad (i = 1, 2, 3) \tag{A10a}$$

and

$$\overline{X}_{ij} = (\det \mathbf{G})^{-2} g^2 u_i u_j - (\det \mathbf{G})^{-1} g(n_i u_j + n_j u_i) - Q_{ij}^{-1} = 0 \quad (i \neq j = 1, 2, 3). \tag{A10b}$$

The trace of $\overline{X}$ can be constructed and rearranged to yield:

$$(\det \mathbf{G})^{-2} g^2 = Q_{11}^{-1} + Q_{22}^{-1} + Q_{33}^{-1} - 2(\det \mathbf{G})^{-1} - 1. \tag{A11}$$

Elimination of g^2 from Equations A6 and A11 results in the following relation for **Q**:

$$(\det \mathbf{G})^{-1}(Q_{11} + Q_{22} + Q_{33} - 1) = (\det \mathbf{G})\left(Q_{11}^{-1} + Q_{22}^{-1} + Q_{33}^{-1} - 1\right). \tag{A12}$$

The lattice invariant shear **V** of magnitude v on a plane of the unit normal **o** in the unit direction **l** is given as:

$$\mathbf{V} = \mathbf{I} + v\mathbf{l} \otimes \mathbf{o} \tag{A13a}$$

and

$$\mathbf{V}^{-1} = \mathbf{I} + v\mathbf{l} \otimes \mathbf{o}. \tag{A13b}$$

Substitution of Equations A13a and A13b respectively in Equations A3 and A8 and then in Equation A12 yields the following quadratic equation for v:

$$\begin{aligned} v^2\{&(\det \mathbf{G})^{-1}(\mathbf{l} \cdot \mathbf{P}^2\mathbf{l}) - (\det \mathbf{G})(\mathbf{o} \cdot \mathbf{P}^{-2}\mathbf{o})\} \\ &+ 2v\{(\det \mathbf{G})^{-1}(\mathbf{o} \cdot \mathbf{P}^2\mathbf{l}) + (\det \mathbf{G})(\mathbf{l} \cdot \mathbf{P}^{-2}\mathbf{o})\} \\ &+ \{(\det \mathbf{G})^{-1}\mathrm{tr}\,(\mathbf{P}^2) - (\det \mathbf{G})\,\mathrm{tr}(\mathbf{P}^{-2}) - (\det \mathbf{G})^{-1} \\ &+ (\det \mathbf{G})\} = 0 \end{aligned} \tag{A14}$$

where $\mathrm{tr}(\mathbf{P}^2) = P_{11}^2 + P_{22}^2 + P_{33}^2 + 2P_{12}^2 + 2P_{23}^2 + 2P_{31}^2$ and $\mathrm{tr}(\mathbf{P}^{-2})$ is defined in an analogous way. For each **l**/**o** pair, Equation A14 gives two values for v which, in turn, via Equation A13 yield two possible lattice invariant shears **V** and, hence, two possible values for **Q**. Once **G** is determined, the IPS shear unit direction **m** and the shear magnitude γ^{tr} are determined as:

$$\gamma^{\mathrm{tr}}\mathbf{m} = g\mathbf{u} - (\det \mathbf{G})\mathbf{n}. \tag{A15}$$

In summary, the basic crystallographic features of a martensitic transformation can hence be determined using the following procedure:

1. Lattice parameter and lattice correspondence of the parent phase and martensite are first established, and the pure strain **P** and the martensite/parent phase volume ratio ($\det \mathbf{G}$) calculated.
2. The unit plane normal **o** and the corresponding unit shear direction **l** for the lattice invariant shear **V** are selected using the available experimental data.
3. $\det(\mathbf{G})$, **P**, **o** and **l** are substituted into Equation A14 to obtain the magnitude of the lattice invariant shear v.
4. v is substituted in Equation A13 to obtain **V**.
5. **P** and **V** are substituted in Equation A3 to obtain **Q**.
6. $\det\mathbf{G}$ and **Q** are next substituted in Equation A6 to obtain g.
7. **Q** is substituted in Equation A7 to obtain **n**.
8. g, **n** and **Q** are substituted in Equation A5 to obtain **u**.
9. g, **n** and **u** are substituted in Equation A1 to obtain **G**.
10. γ^{tr} and **m** are determined using Equation A15.

In general, for each combination of $\det(\mathbf{G})$, **P**, **o** and **l**, there are two values of v and four values for **G**.

Acknowledgements

This material is based upon work supported by the National Science Foundation under grant number DMR–9906268 and CMS–9531930 and by the U. S. Army

Research Office under grant number DAAH04–96–1–0197. The authors are indebted to Drs. Bruce A. MacDonald and Daniel C. Davis of NSF and Dr. Kathryn V. Logan of ARO for continuing interest in the present work. The authors are also indebted to Professor Surya Kalidindi for an inspiring discussion. The support of the office of High Performance Computing Facilities at Clemson University is acknowledged.

References

1. G. B. OLSON, K. TSUZAKI and M. COHEN, *Materials Research Symposium Proceedings* **57** (1987) 129.
2. A. G. EVANS and R. M. CANNON, *Acta Met.* **34** (1986) 761.
3. G. B. OLSON, in Sagamore Army Materials Research Conference Proceedings, 1987, edited by G. B. Olson, M. Azrin and E. S. Wright, p. 3.
4. M. GRUJICIC and P. DANG, *Mater. Sci. Eng.* **A224** (1997) 187.
5. B. BUDIANSKY, J. W. HUTCHINSON and J. C. LAMBROPOULOS, *Int. J. Solids Structures* **19** (1983) 337.
6. C. L. HOM and R. M. MCMEEKING, *ibid.* **26** (1990) 1211.
7. M. GRUJICIC and N. SANKARAN, *ibid.* **34** (1997) 4421.
8. *Idem., Int. J. Fracture* **83** (1997) 337.
9. S. KALIDINDI, *J. Mech. Phys. Solids* **46** (1998) 267.
10. R. J. ASARO and A. NEEDLEMAN, *Acta Met.* **33** (1985) 923.
11. G. B. OLSON and A. L. ROITBURD, in "Martensite," edited by G. B. Olson and W. S. Owen (ASM International, The Materials Information Society, 1992) p. 149.
12. I. W. CHEN, Y. H. CHIAO and K. TSUZAKI, *Acta Met.* **33** (1985) 1847.
13. T. W. DUERIG, G. T. TERLINDE and J. C. WILLIAMS, *Metal Trans. A* **11A** (1980) 1987.
14. A. G. CROCKER, Journal de Physique, Colloque C4, Supplement au no **12** (1982) C4–209.
15. J. C. WILLIAMS, in "Titanium Science and Technology, Vol. 3," edited by R. I. Jaffee and H. M. Burte (1973) p. 1433.
16. J. S. BOWLES and J. K. MACKENZIE, *Acta Met.* **2** (1954) 129.
17. Y. ZHANG, PhD thesis in Progress, Clemson University, May 1999.
18. Abaqus Standard Theory Manual, Version 5.7, Hibbit, Karlson and Sorensen, Inc., Providence, RI, 1997.
19. J. S. KALLEND, U. F. KOCKS, A. D. ROLLETT and J. R. WENK, popLA: The Preferred Orientation Package from Los Alamos, 1994.

Received 30 June 1999
and accepted 8 March 2000